RSC Advances

PAPER

View Article Online
View Journal | View Issue

Cite this: *RSC Adv.*, 2025, **15**, 24192

Zinc(II) ion detection and fluorescence emission properties of a diaminomaleonitrile-derived unsymmetrical Schiff base ligand†

Tesfa Oluma Fufa, Hongwei Ma, Ali R. Ayub, Karim Y. Nabat, Yaqoot Khan and Hui Li *

A novel Schiff base ligand, 2-amino-3-(((*Z*)-2,5-dihydroxybenzylidene)amino)maleonitrile hemihydrate ($C_{11}H_8N_4O_2\cdot\frac{1}{2}H_2O$ or **H_2L**), was synthesized by a condensation reaction of diaminomaleonitrile and 2,5-dihydroxybenzaldehyde in ethanol. Its crystal structure, fluorescence (FL) emission and Zn(II)-detection properties were studied. The crystal structure of **H_2L** belongs to a face-centered orthorhombic space group (*Fdd2*), confirming its crystalline nature. **H_2L** emitted green-colored fluorescence in MeCN, EtOH, and DMF, with varying FL yields of 0.53, 0.68, and 0.95, respectively. This suggests that the solvent environment plays a crucial role in modulating the FL properties of **H_2L**. In DMF, the gradual addition of Zn(II) to the **H_2L** solution resulted in a color change from yellow to orange, accompanied by the appearance of new absorbance bands at 494 nm and two isosbestic points at 300 and 440 nm. These phenomena were not observed either in MeCN or EtOH, indicating that Zn(II)-**H_2L** binding was more pronounced in DMF. Thus, **H_2L** demonstrated sensitive Zn(II) binding, with a 1 : 1 binding stoichiometry, a high binding constant (3.745×10^7 μM^{-1}), and a low limit of detection (3.455×10^{-6} μM). Overall, the findings highlight the potential of the novel crystalline **H_2L** for efficient FL emission and sensitive Zn(II) detection in DMF, suggesting its potential utilization for fabricating light-emitting organic devices and metal-ion sensors.

Received 14th May 2025
Accepted 26th June 2025

DOI: 10.1039/d5ra03383g

rsc.li/rsc-advances

1. Introduction

In recent years, Schiff bases have received considerable attention in coordination chemistry and materials science due to their ability to bind metal ions and their interesting optical properties.[1–3] In particular, aromatic Schiff bases, such as *ortho*-hydroxybenzaldehyde groups, have demonstrated strong fluorescence responses through excited-state intramolecular proton transfer (ESIPT).[4] ESIPT-active molecules offer distinctive features, such as a large Stokes shift, dual spectra, ultrafast recovery, and sensitivity to the surrounding environment.[5] Diaminomaleonitrile-derived Schiff bases have shown remarkable properties in various studies[6–10] through their electron-donating and -withdrawing groups, which can modify the electronic properties of the resulting compounds.

Zn is an essential trace element in many environmental and biological processes, but an imbalance in Zn(II) ion concentration[11] can cause health problems, particularly when Zn is ingested in human nutrition.[12] The WHO's[13] recommended maximum level of Zn(II) in drinking water is 46 μM. Consequently, several complex analytical detection methods[14] have been developed and applied to detect Zn. Thus, the development of novel molecules and simple methods[15–18] to detect Zn ions is relevant in both environmental and health/medical fields.[19–21] Usually, it is difficult to detect Zn(II) in coordination complexes within the visible range due to the filled 3d orbitals and the weak polarizability of the solvent used during the study. The ligand fields around Zn(II) create highly symmetric environments that can suppress electronic transitions, leading to "spectral silence" in spectroscopic analyses.[22,23]

To address the aforementioned issues, we developed a novel diaminomaleonitrile-derived unsymmetrical Schiff base, namely, 2-amino-3-(((*Z*)-2,5-dihydroxybenzylidene)amino)maleonitrile hemihydrate (**H_2L**). The developed **H_2L** is highly polar due to its multiple donor–acceptor functional groups, which contribute to its supramolecular interactions, fluorescence emission, and ionic metal binding. The fluorescence emission and Zn(II) detection potentials of **H_2L** were evaluated in MeCN, EtOH and DMF. The results indicated that **H_2L** emitted green light fluorescence in each solvent, with varying fluorescence yields. In DMF, the gradual addition of Zn(II) into **H_2L** solution resulted in a color change from yellow to orange, accompanied by the appearance of new absorbance bands and isosbestic

Key Laboratory of Clusters Science of Ministry of Education, School of Chemistry and Chemical Engineering, Beijing Institute of Technology, 100081, Beijing, P. R. China. E-mail: lihui@bit.edu.cn; Tel: +8613910835773

† Electronic supplementary information (ESI) available. CCDC 2402446. For ESI and crystallographic data in CIF or other electronic format see DOI: https://doi.org/10.1039/d5ra03383g

points, which were not observed either in MeCN or EtOH. This suggests that the solvent environment plays a crucial role in modulating the properties of **H_2L**. This study offers valuable insights into the design of future materials for applications in areas such as fluorescence,[24] bio-detection and environmental monitoring,[22] and organic electronics and photonic devices.[25]

2. Experimental section

2.1. Synthesis and recrystallization

H_2L was synthesized according to the previous references.[9,26] All the chemicals used in the experiments were purchased from Sigma-Aldrich or Merck.

In the synthesis, into two beakers each containing EtOH (50 mL), 0.03903 g of 2,5-dihydroxybenzaldehyde (2,5-DHBA) and 0.03055 g of diaminomaleonitrile (DAMN) were added, respectively. The mixtures were stirred on a hot plate for 0.5 h. The first solution was then transferred into a 250 mL round-bottom flask and the second solution was added dropwise followed by 3 mL of AcOH. The mixture was refluxed for 4 h, after which it was allowed to cool to room temperature (RT) for 2 h. The resulting precipitate was filtered by gravity filtration, washed with excess EtOH, and dried at RT for 2 days, giving 0.06 g of **H_2L** (Fig. S1d and S2a†), as obtained by weighing on an analytical balance.

Single crystals of **H_2L** were grown based on a previous study.[27] In brief, in a 25 mL beaker, 0.0664 g of **H_2L** was dissolved in H_2O (3 mL) and MeCN (5 mL), stirred for 0.5 h at 80 °C, filtered by gravity filtration, covered with a needle-punctured para-film and allowed to stand in a cool place without any perturbation. After 10 days, suitable single crystals were obtained (Fig. S2b†).

2.2. Characterization

2.2.1 Single crystal X-ray diffraction. A suitable single crystal of **H_2L** ($0.35 \times 0.30 \times 0.25$ mm^3) was carefully extracted/selected from the growth medium using tweezers, mounted on the X-ray diffraction (XRD) instrument sample holder using a minimal amount of adhesive, and the data were collected on a Bruker D8 Venture diffractometer equipped with MoKα radiation ($\lambda = 0.71073$ Å).

2.2.2 Powder X-ray diffraction. Using mortar and pestle, the obtained single crystals were ground into a fine powder to ensure random orientation of crystallites and to enhance the interaction with the X-ray beam. Then, the powder XRD patterns were recorded on a Bruker D8 Advance diffractometer equipped with monochromatic CuKα radiation ($\lambda = 1.5418$ Å), operated at 40 kV and 30 mA, and the diffraction intensity data were obtained by scanning at 2 min^{-1}.

2.2.3 TGA analysis. First, 9.1 mg of the **H_2L** sample was weighed on an analytical balance, and then placed on an alumina crucible, and heated from 40 °C to 800 °C at a heating rate of 10 °C min^{-1} using a NETZSCH STA 449F5 instrument under an inert atmosphere.

2.2.4 UV-vis spectra. Stock solutions of **H_2L** (2.5×10^{-5} M) and $Zn(NO_3)_2 \cdot 6H_2O$ (2.5×10^{-3} M) were separately prepared in DMF, EtOH and MeCN. The concentration of **H_2L** was kept constant and different volumes of Zn(II) ions (from 06 to 60 μL) were added to the **H_2L** solution. The absorbance spectra were performed using a TU-1950 UV-vis spectrophotometer.

2.2.5 Fluorescent spectra. A stock solution of **H_2L** (2.5×10^{-5} M) was prepared in DMF, EtOH and MeCN, respectively. At RT, the FL emission spectra were recorded using a Hitachi F-7000 FL spectrophotometer. Then, 3 mL of **H_2L** solution was placed in a quartz cell (1 cm^2), and its FL spectrum was measured at $\lambda_{ex} = 400$ nm, with an excitation slit width of 5.00 nm, emission slit width of 5.00 nm, at a scan rate of 2400 nm min^{-1} and a PMT voltage of 850 V. The spectrum of the solution was obtained between 400 and 600 nm. The FL emission yield of **H_2L** was calculated relative to RhB ($\lambda_{ex} = 350$ nm, $\lambda_{em} = 703$ nm, $\Phi_{FL} = 0.65$, in EtOH at 25 °C)[42] as standard following the formula given by Crosby and Demas:[43]

$$\Phi_{FL} = \Phi_s \left(\frac{F_x}{F_s}\right)\left(\frac{f_s}{f_x}\right)\left(\frac{I_s}{I_x}\right)\left(\frac{{\eta_x}^2}{{\eta_s}^2}\right) \quad (1)$$

where Φ, x, s, F, η and f are the FL yield, sample, standard, area under the FL spectrum (Fig. S8–S11†), refractive index of the solvent used and absorption factor at λ_{em}, respectively. Also, $f = 1 - 10^{-A}$, where A is the absorbance (Fig. S5†).

2.2.6 ^{1}H NMR spectra. At 25 °C, 5 mg of **H_2L** was dissolved in 600 μL of DMSO-d_6 solvent and then transferred into a clean and dry NMR tube. The NMR tube was sealed with a plug to prevent evaporation of the solvent and contamination. The spectrum of **H_2L** was recorded on a Bruker AV 400 spectrometer using TMS standard. 6.79 (d, $J = 2$ Hz, 1H, C(3)H), 7.38 (dd, $J = 2$ and 9 Hz, 1H, C(4)H), 8.50 (l, 2H, NH_2), 7.83 (s, $J = 9$ Hz, 1H, C(6)H), 8.95 (l, 1H, OH), 9.76 (s, 1H, N=CH) and 10.33 (l, 1H, OH).

2.2.7 Elemental analysis. Here, 2 mg of **H_2L** was weighed and elemental analysis was performed on a PerkinElmer 240 Elemental Analyzer, and the proportions of C (57.89%), H (3.53%), N (24.55%) and O (14.02%) were obtained.

2.2.8 FT-IR measurements. Using a mortar and pestle, 1 mg of **H_2L** was finely crushed along with 100 mg of KBr to make KBr pellets by compressed them into a pellet using a hydraulic press. The spectral data of the pellets were then recorded on a Bruker AlPHA FT-IR spectrometer, with peaks observed at 3466–3337 cm^{-1} (related to –OH and NH_2), 2240 and 2228 cm^{-1} (related to –CN), and 1627 cm^{-1} (related to –HC=N–).

3. Results and discussion

3.1. Synthesis

Following the previous references,[9,26] **H_2L** (Scheme 1) was successfully synthesized *via* a condensation method by refluxing equal moles of diaminomaleonitrile (DAMN) and 2,5-hydroxybenzaldehyde (2,5-DHBA) in EtOH and AcOH. The solution was then cooled at RT, filtered under vacuum, washed with ethanol, dried at room temperature, and finally the product was recrystallized from MeCN/H_2O solution.

The percentage yield (Y%) of **H_2L** was calculated using the balanced reaction equation, theoretical yield (TY), actual yield (AY), limiting reactant mole (n_{LR}), LR stoichiometric coefficient

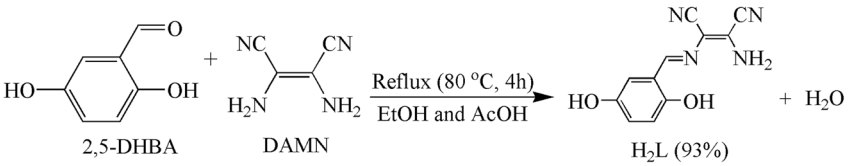

Scheme 1 Schematic representation of the condensation synthesis of H_2L.

(k_{LR}) and molar mass of the product (*i.e.*, $M_{H_2L} = 228.21$ g) using eqn (2) and (3).

$$C_7H_6O_3 + C_4N_4H_4 \xrightarrow{\Delta} C_{11}H_8N_4O_2 + H_2O \quad (2)$$

$$Y = \frac{AY}{TY} \times 100 = \frac{AY}{n_{LR} \times \frac{k_P}{k_{LR}}} \times 100 \quad (3)$$

3.2. Crystal structure

The crystal structure of **H_2L** was determined using Olex2 (ref. 28) with the SHELXT[29] structure solution program using Intrinsic Phasing and refined with SHELXL[30] using least squares minimization. The SC XRD analysis proved that **H_2L** was crystallized as a hemihydrate ($C_{11}H_8N_4O_2 \cdot \frac{1}{2}H_2O$) and belonged to a face-centered orthorhombic space group (*Fdd*2). Fig. 1a, Tables 1 and S2–S4† present the molecular structure, crystal data and atomic parameters, respectively. The molecule adopted a planar conformation as a result of the strong H-bonding between the H(1) and N(1) with a distance of 1.985 Å and an angle of 138.75°. Also, the flat nature of **H_2L** may be due to the extended π-conjugation to the peripheral nitrile groups. This allowed us to investigate the supramolecular structures, which have been reported to directly impact the fluorescence properties of compounds.[44]

Notably, the crystal packing exhibited strong H-bonding (1.94–2.49 Å, Fig. 1b) and π–π stacking (3.375 Å, Fig. 1c) between the adjacent **H_2L** molecules, which may contribute to strong fluorescence properties by allowing a greater excitation energy. In rigid structures, molecular vibrations and rotations are restricted, which reduces the non-radiative relaxations where the energy absorbed is dissipated as heat instead of being emitted as fluorescence. By reducing the non-radiative pathways through increasing the rigidity, the fluorescence potentials can be increased. Due to their orthorhombic symmetry, the **H_2L** molecules were arranged in offset parallel along the crystallographic axis in order to minimize the repulsive forces between the electron-dense regions and the voids between the rings (Fig. 1c). Such condensed molecular arrangements are beneficial for efficient electron transfer among orbitals and is recommended for strong fluorescence emission, particularly in polar organic solvents.

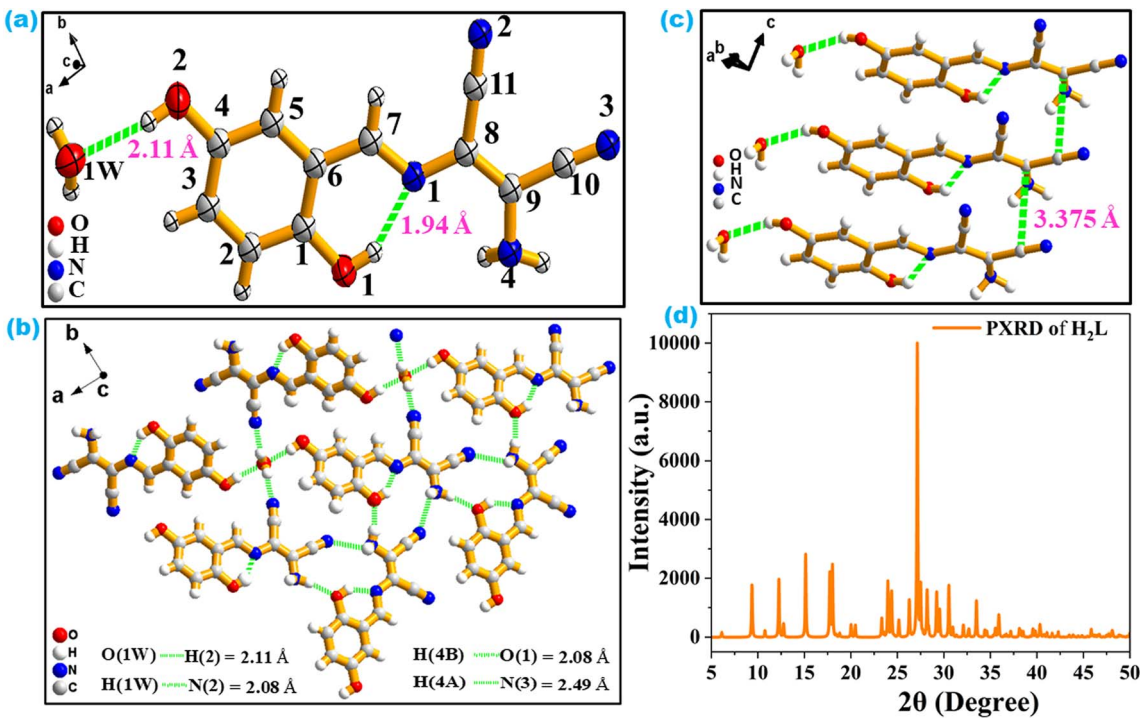

Fig. 1 SC structure (a), H-bonding (b), π–π interactions (c), and PXRD pattern (d) of H_2L.

Table 1 Crystal data and structural refinement of H_2L

Parameter	Data
CCDC number	2402446
Molecular formula	$C_{11}H_8N_4O_2 \cdot \frac{1}{2}H_2O$
Formula weight (g mol^{-1})	237.22
Temperature (K)	296.15
Crystal system	Orthorhombic
Space group	*Fdd2*(43)
Unit cell dimensions (Å)	$a = 19.936(7)$, $b = 57.668(19)$, $c = 3.7770(13)$
Unit cell angles (°)	$\alpha = \beta = \gamma = 90$
Unit cell volume (Å^3)	4342(3)
No. of molecules per unit cell, Z	16
Calculated density, ρ_{calc} (g cm^{-3})	1.451
Linear absorption coefficient, μ (mm^{-1})	0.108
F (000)	1968.0
Crystal size (mm^3)	0.35 × 0.3 × 0.25
Radiation	MoKα ($\lambda = 0.71073$)
2θ Range for data collection (°)	2.824 to 52.48
Index ranges	$-19 \le h \le 15$, $-44 \le k \le 56$, $-3 \le l \le 3$
Reflections collected	2199
Independent reflections	1037 [$R_{int} = 0.0743$, $R_{sigma} = 0.1073$]
Data/restraints/parameters	1037/1/165
Goodness-of-fit on F^2	1.068
Final R indexes [I ≥ 2σ (I)]	$R_1 = 0.0675$, $wR_2 = 0.1491$
Final R indexes [all data]	$R_1 = 0.1008$, $wR_2 = 0.1769$
Largest diff. peak/hole/e Å^{-3}	0.27/−0.25
Flack parameter	−8.8(10)

The PXRD pattern of **H_2L** showed a series of sharp peaks at 2θ angles corresponding to the interplanar distances (d) according to Bragg's law ($n\lambda = 2d \sin\theta$), Fig. 1d. Thus, the PXRD technique proved the crystallinity and phase purity of **H_2L**, which also agreed with the elemental analysis data.

Furthermore, the structure of **H_2L** was supported by various analytical techniques, including FT-IR, ^{1}H NMR and elemental analysis. The elemental analysis showed the presence of C (57.89%), H (3.53%), N (24.55%) and O (14.02%), consistent with the structure. Also, the calculation of the empirical formula of**H_2L** based on these aforementioned percentages confirmed its purity. The 1H NMR spectrum (Fig. S3†) of **H_2L** in DMSO-d6 showed a singlet at 10.33 ppm (H(1)) and peaks at 9.76, 8.95, 8.50, and 7.83–6.79 ppm corresponding to H(7), H(2), H(4A & 4B), and H(5, 3 & 2), respectively. The downfield shift at 10.33 ppm was due to H(1), which participated in intramolecular hydrogen bonding. The FT-IR spectrum of **H_2L** in a KBr pellet (Fig. S4†) provided evidence of the mono-imine nature (–HC═N– at 1627 cm^{-1}), while the nitriles (–HC═N–) stretching modes were split into two bands at 2228 and 2240 cm^{-1}, which were assigned to the symmetric and asymmetric stretching modes, respectively.[49] This was in contrast to the single band observed for the symmetric di-imine nature (at 2210 cm^{-1}).[31] Also, the narrow peaks between 3197 and 3466 cm^{-1} were attributed to the –(H–N–H) and –(O–H) stretching vibrations.[26]

To investigate the thermal stability, a sample of **H_2L** was heated from 40 °C to 800 °C at a heating rate of 10 °C min^{-1} under an inert atmosphere, Fig. S13.† The graph's small decline (40–150 °C) indicated the weight loss percentage of hemi-water (4.43%), which was observed in the single-crystal molecular structure, while the observation of a plateau region (150–250 °C) suggested the thermal stability of the ligand after the loss of hemi-water. The next significant weight loss percentage seen at 250 °C was related to the loss percentage of an amine group (12.32%) while the final weight losses percentage (beyond 250 °C) may be due to the gradual decomposition of the other organic moieties.

3.3. Fluorescence study

After determining the crystal structure, we investigated the UV-vis absorbance and fluorescence emission spectra of **H_2L** in various polar organic solvents, namely, DMF, EtOH, and MeCN, because it is known that the electronic transitions of Schiff bases are strongly influenced by the nature of the medium.[32] In each solution, the color of **H_2L** appeared yellow under room light (see the inset image of Fig. 2a) and green under ultraviolet light (see the inset image of Fig. 2b).

First, we studied the absorbance spectra (Fig. 2a) and found that the maximum absorbance wavelength was shifted from 342 nm to 402 nm, which may have been due to the excited-state dipole moment changes, H-bonding strengths (Fig. S6†), and/or due to excited-state protonation.[33,34] The influence of the solvents on **H_2L** absorbance increased in order of: MeCN (342 nm) < EtOH (348 nm) < DMF (402 nm). Thus, DMF was the best polar aprotic solvent in this case.[35,36] The λ_{max} redshift (402 nm) indicated that DMF could strongly stabilize the **H_2L** excited state. In DMF and between 280 and 600 nm, the absorption spectra of **H_2L** showed two absorption peaks (352 and 402 nm),

which were due to the intra-ligand charge transitions (ILCT or n → π*).[37,46]

Next, we studied the FL emission spectra (Fig. 2b) of **H_2L** in each solvent. Notably, the **H_2L** sample was suspended in each solvent with a concentration of 25 μM, and then excited at 400 nm. The samples exhibited green emission at 544 nm in DMF, 533 nm in EtOH, and 521 nm in MeCN. The inset image in Fig. 1b confirmed this result under UV light (365 nm) irradiation. Further, in each solvent, the FL spectrum of **H_2L** revealed a systematic Stokes's shift ($\Delta\lambda = \lambda_{em} - \lambda_{ab} = 142$ nm in DMF, 132 nm in EtOH and 121 nm in MeCN), which reflected the charge-separated nature of the excited states.[38,39] Thus, **H_2L** showed the highest charge separation and highest fluorescence in the presence of DMF, whereas the other two solvents were relatively less polar. In each solvent, the weak band around 455 nm was due to some excited enol emission and the strong peaks at 521 nm in MeCN, 533 nm in EtOH and 544 nm in DMF were due to the excited keto emission of **H_2L**. These dual emissions are characteristics of ESIPT-exhibiting molecules.[40,41] In DMF solution, the emission band of **H_2L** at 544 nm was further redshifted and more intense compared to in EtOH and in MeCN, indicating a strong preference for the excited keto emission, which may be due to its highest refractive index, highest dielectric constant, most polar nature and high polarizability. Thus, the spectral redshifts observed at $\lambda_{ab} = 402$ nm and at $\lambda_{em} = 544$ nm suggest that DMF could strongly stabilize **H_2L** (Fig. 2).

In the solution state, the observed dual peaks in the above spectra (Fig. 1a and b) confirmed that **H_2L** existed in two isomeric forms (*i.e.*, enol tautomeric form, see Fig. S12a,† and the keto tautomeric form, see Fig. S12b†). Following eqn (1), the calculated FL emission yields of **H_2L** were 0.53 in MeCN, 0.68 in EtOH, and 0.95 in DMF.

Both the UV-vis and FL spectral analyses proved that DMF was the strongest electron donor compared to EtOH and MeCN. The amide group in DMF has a highly polarizable oxygen atom with lone pairs, making it a strong Lewis base. This allows DMF to donate electrons effectively to the electron-deficient regions of **H_2L**, stabilizing the Lewis acidic sites in the compound. EtOH was an intermediate electron donor. Although it has polarizable oxygen atom with lone pairs, its primary interactions involve donating protons rather than electrons because it is a protic solvent with an –OH group. This limits its electron-donating capacity compared to DMF. MeCN was the weakest electron donor. The nitrile group in acetonitrile is a weak Lewis base due to the electronegative sp-hybridized nitrogen, which poorly donates electrons. It primarily acts as a polar aprotic solvent with low basicity.

The fluorescence emission mechanisms of **H_2L** are shown in Fig. 3. Upon photo-irradiation, the ground state enol form of **H_2L** (E) relaxes to its excited-state enol form (E*), from where some of the absorbed photons return to the E while emitting E*-FL and the others relax to the excited-state keto form (K*) *via* an ESPT process due to the redistribution of electronic charges. Then, K* decays to K while emitting K*-FL. Finally, K will turn back to E by a reverse proton transfer (RPT).[45] This overall processes are called photo-tautomerism.

Furthermore, based on the former literature,[45] in order to understand the dual-fluorescence emission, reactive regions and frontier orbitals of **H_2L**'s tautomeric forms, we performed density functional theory (DFT) calculations using the Gaussian

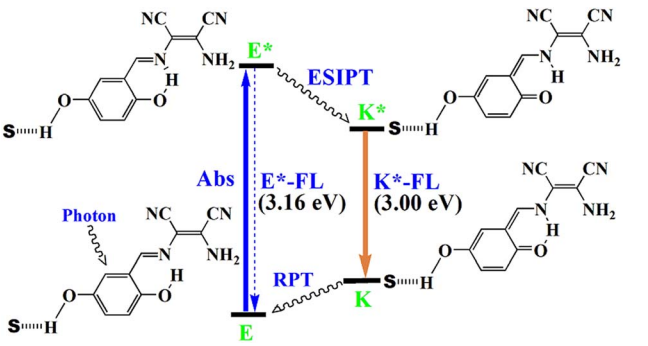

Fig. 3 Fluorescence emission mechanisms of H_2L *via* ESIPT; S = DMF, EtOH or MeCN.

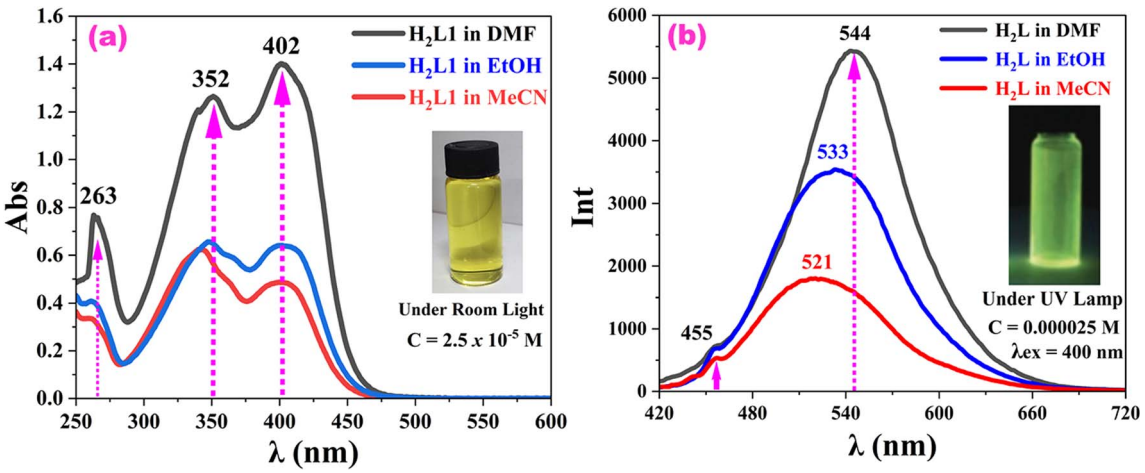

Fig. 2 UV-vis absorbance (a) and FL emission (b) spectra of H_2L in different solvents.

09 software package at the B3LYP/6-31G(d) level. The molecular electrostatic potential of **H_2L** (Fig. S12a and b†) showed the nucleophilic region was near the oxygen atoms and nitrogen atoms and these regions were significant for accepting and donating hydrogen bonds within the supramolecular structure. The blue color in the figures indicates the electron-accepting region and the red-color indicates the electron-donating region. The HOMO was mainly distributed on the benzene ring and C–C double bonds, while the LUMO isosurface was mainly located around the N of the DAMN skeleton. When electrons absorb energy, they move from the HOMO to LUMO. The calculated energy gaps were 3.16 eV for the **H_2L** enol form (see Fig. S12c†) and 3.00 eV for the **H_2L** keto form (see Fig. S12d†), which confirmed the reliability of the aforementioned dual-fluorescence emission mechanisms. As a result, the observed fluorescence property of the **H_2L** supra-molecules were dominated by the keto-fluorescence emission rather than the enol-fluorescence emission, particularly in DMF solution.

3.4. Zn(II) selectivity study

To assess the selectivity of **H_2L** for Zn(II), various experiments were conducted by introducing potential ions such as Cu(II), Ni(II) and $[NO_3]^-$ into a solution of **H_2L** in 50% DMF/tris–HCl buffer (pH 7.4, 25 °C), following established protocols.[51] Spectrophotometric titrations of **H_2L** with Zn(II) ions produced a redshifted absorbance band (at 494 nm) compared to the absorption bands of the competing ions (Fig. S17a, S18c and S19e†). Also, the spectrofluorometric titrations of **H_2L** with Zn(II) induced FL TURN-ON (at $\lambda_{em} = 544$ nm and $\lambda_{ex} = 400$ nm), attributed to structural-rigidification and non-radiative-decay suppression *via* a chelation-enhanced fluorescence (CHEF) mechanism. The solution was accompanied by a clear color change from bright-orange to bright-green under a 365 nm UV lamp, Fig. 4b(2). Hence, the emission occurred from a ligand-centered excited state ($\pi \rightarrow \pi^*$) and was more efficient due to the reduced vibrational relaxations.

Conversely, the paramagnetic Cu(II) and Ni(II) ions caused FL TURN-OFF (Fig. S17(b) and S18(d)†), *via* photoinduced electron transfer (PET) and d–d transition-mediated non-radiative decay pathways. Their respective solutions were accompanied by weak-green emission under a 365 nm UV lamp, Fig. S16(e and f).† However, the nitrates did not produce effective spectral (Fig. S19(e and f)) or color (Fig. S16(g)†) responses under the same experimental conditions as they were incapable of coordinating with the ligand's donor sites. This distinct ion-specific behavior demonstrates **H_2L**'s potential as a selective FL sensor for Zn(II)(TURN-ON FL). Zn(II) is a borderline Lewis acid, which meant it could bind well with the nearby donor sites of **H_2L** in a highly polar DMF and caused FL TURN-ON. Also, Cu(II) and Ni(II) are borderline acids but caused FL TURN-OFF due to their paramagnetic effects, which promoted intersystem crossing

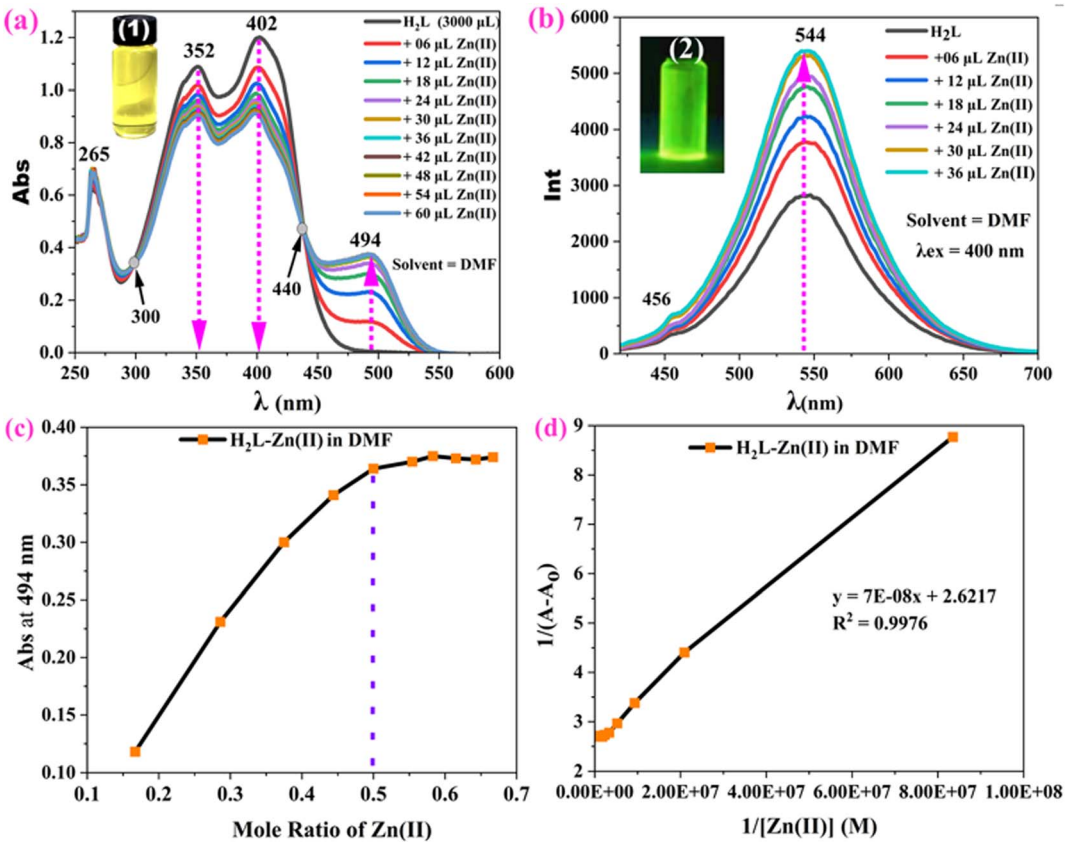

Fig. 4 UV-vis absorbance spectra (a), FL emission spectra (b), Job's plot (c), and Benesi–Hildebrand plot (d) of H_2L with Zn(II) in DMF. Insets show the color changes of H_2L upon Zn(II) addition under natural light (1) and UV light (2).

(ISC) from the ligand's singlet excited state (S_1) to the metal's triplet state (T_1).[50] Overall, the selectivity of **H_2L** towards Zn(II) was demonstrated by a redshift in the UV-vis spectra (at λ_{abs} = 494 nm), by FL TURN-ON (at λ_{em} = 544 nm) and by the color change from right-orange to bright-green under a UV lamp.

Further, to assess the selectivity of **H_2L** for Zn(II), fluorometric competitive binding experiments were conducted by introducing the potential interferent ions Cu(II), Ni(II) and $[NO_3]^-$ into a solution containing **H_2L** and Zn(II) (Fig. S20†). Upon adding 60 μL of Cu(II) to the **H_2L**-Zn(II) mixture, the fluorescence intensity dropped sharply to 613 due to Cu(II)'s competitive binding and paramagnetic quenching. For Ni(II), the fluorescence decreased moderately to 2105, reflecting the partial Zn(II) displacement and weaker quenching. In contrast, $[NO_3]^-$caused no significant change (2970 *vs.* 3000), as it could not coordinate with **H_2L**. Thus, the interference order was: $[NO_3]^- \ll$ Ni(II) < Cu(II).

3.5. Zn(II) binding study

Although the single-crystal structure determination of the Zn(II)-**H_2L** complex was unsuccessful despite repeated efforts, UV-vis titration experiments confirmed the coordination interaction between **H_2L** and Zn(II). Upon the gradual addition of Zn(II) to **H_2L** in DMF (Fig. 4a), EtOH (Fig. S14†), and MeCN (Fig. S15†), the yellow solution turned orange in each solvent. In DMF, the absorbance bands of **H_2L** (402 and 352 nm) decreased, accompanied by the appearance of two isosbestic points (440 and 300 nm) and a new band at 494 nm. These spectral changes indicated Zn(II) binding to the three donor sites of **H_2L**, facilitated by the removal of the acidic proton H(1) and the basic proton H(4A) (Fig. 5). The presence of isosbestic points suggests the direct formation of a stable complex without intermediates. The new band at 494 nm likely arose from ligand-to-metal charge transfer (LMCT),[24] where electrons shifted from the donor atoms (O/N) to Zn(II) ($3d^{10}$ $4s^0$) or from Zn(II) ($3d^{10}$) to **H_2L**, enhanced by the two strong electron-withdrawing –CN groups.

To determine the **H_2L**-Zn(II) binding stoichiometry, Job's plot analysis was performed using the continuous variation method. As shown in Fig. 4c, the absorbance measured at 494 nm exhibited a maximum at a Zn(II) mole fraction ($\chi_{Zn(II)}$) of 0.5, confirming a 1 : 1 binding ratio. The data were analyzed according to eqn (4) below.[47]

$$\Psi_{Zn(II)} = \frac{n_{Zn(II)}}{n_{Zn(II)} + n_{\mathbf{H_2L}}} \quad (4)$$

where $n_{Zn(II)}$ is the number of moles of Zn(II), and $n_{Zn(II)}$ is the number of moles of **H_2L**.

The binding constant ($3.745 \times \mu M^{-1}$) of Zn(II) with H_2L was calculated using a Benesi–Hildebrand plot (Fig. 4d) or (eqn (5)).[15]

$$\left(\frac{1}{\bar{A} - A_O}\right) = \frac{1}{K_a(A_{max} - A_O)}\left(\frac{1}{[Zn^{2+}]}\right) + \left(\frac{1}{A_{max} - A_O}\right) \quad (5)$$

where A_O is the absorbance of **H_2L** in the absence of Zn^{2+} at 494 nm, $\bar{A}$ is the absorbance mean of the mixtures, A_{max} is the absorbance of the mixtures at the highest Zn^{2+}, $[Zn^{2+}]$ is the highest concentration of Zn(II) and K_a is a binding constant, which was also calculated from the slope (m) of a straight line plot of $1/(A - A_0)$ and 1/[Zn(II)], where K_a was determined from the intercept/slope ratio.[48]

The detection limit (DL) of Zn(II) by **H_2L** was calculated as 3.455×10^{-6} μM using the standard deviation (σ) of the UV-vis absorbance of **H_2L** (see Table S1, eqn (S1) and (S2)†) and the slope (m) of the linear regression curve (Fig. 4d), and following eqn (6):[47]

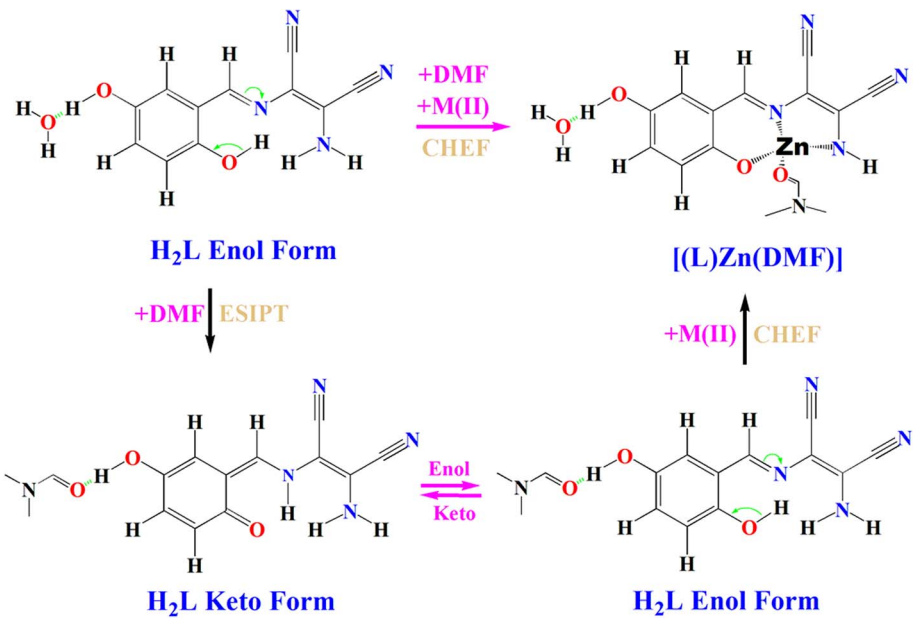

Fig. 5 Sensing mechanisms of H_2L and its Zn(II) coordination in DMF solution.

$$\mathrm{DL} = \frac{3\sigma}{m} \quad (6)$$

The determined limit of detection of $\mathbf{H_2L}$ for Zn(II) was significantly lower than that of the existing ref. 13. This shows the sensitivity of the UV-vis spectroscopy approach and the selectivity of $\mathbf{H_2L}$ in DMF solution.

3.5.1 Sensing mechanisms. The free $\mathbf{H_2L}$ exhibited good FL through an ESIPT process between its nearby hydroxyl and imine groups. Upon Zn(II) addition, a 1 : 1 L-Zn(II)–DMF complex forms *via* coordination to the imine-N, the deprotonated hydroxyl-O and amine-N sites, as shown by the following eqn (7):

$$\mathbf{H_2L} + \mathrm{Zn(NO_3)_2 \cdot 6H_2O} + \mathrm{DMF} \xrightarrow{\Delta} \mathrm{ZnL \cdot DMF} + 2\mathrm{HNO_3} + 6\mathrm{H_2O} \quad (7)$$

The complexation was evidenced by a new absorbance band at 494 nm, clear isosbestic points at 300 and 440 nm, a strong emission band at 544 nm, and a 50 nm Stokes shift (494 → 544 nm). The coordination rigidified the molecular structure, leading to a suppression of ESIPT, reduction of the non-radiative decay pathways and the emergence of strong FL at 544 nm through the CHEF effect. The TURN-ON response and visible color changes confirmed this as a characteristic Schiff base-Zn(II) chemo-sensing system, where metal chelation-enhanced emission by restricting molecular motions and extending π-conjugation. The proposed binding mechanism (Fig. 5) for $\mathbf{H_2L}$ with Zn(II) in DMF is presented below in Fig. 5.

4. Conclusion

A highly crystalline, fluorescent and Zn(II)-detection novel ligand system $\mathbf{H_2L}$ was synthesized by a condensation method and was characterized by various techniques (SC XRD, PXRD, UV-vis, FL, FT-IR, ^{1}H NMR and TGA). $\mathbf{H_2L}$ is highly polar due to its multi donor–acceptor functional groups, which contribute to supramolecular interactions, FL emissions, and metal-ion binding. $\mathbf{H_2L}$ is a yellow solid that is insoluble in water, but highly soluble and stable in polar organic solvents.

In solution, the $\mathbf{H_2L}$ existed as an enol form and keto form. $\mathbf{H_2L}$ was found to be thermally stable up to 250 °C. The FL emission and Zn(II) ion-binding abilities of $\mathbf{H_2L}$ were studied in MeCN, EtOH and DMF, separately. Notably in each solvent, $\mathbf{H_2L}$ emitted green light with varying FL emission yields of 0.9491 in DMF, 0.68 in EtOH and 0.53 in MeCN. The UV-vis and FL spectral analyses prove that DMF was the strongest electron donor compared to EtOH and MeCN due to its highly polarizable oxygen atoms, which can stabilize $\mathbf{H_2L}$.

Furthermore, the binding of $\mathbf{H_2L}$ with Zn(II) was studied by UV-vis spectroscopy in the presence of DMF, EtOH and MeCN, separately. Obviously, there were no spectral changes for EtOH or MeCN in the visible range upon Zn(II) titration with $\mathbf{H_2L}$. However, upon Zn(II) titration with $\mathbf{H_2L}$ in DMF, a new spectral band appeared at 494 nm along with two isosbestic points at 300 and 440 nm. Therefore, for the L-Zn(II)-DMF, a 1 : 1 stoichiometric ratio, a strong binding constant ($3.745 \times 10^7\ \mu M^{-1}$), and a significantly low detection limit ($3.455 \times 10^{-6}\ \mu M$) were calculated. Overall, these findings suggest that the developed $\mathbf{H_2L}$ could be utilized for fabricating green light-emitting organic diodes in the materials science field and for detecting metal ions in the environmental and biological sciences fields.

Data availability

Additional data of this article are provided in the ESI.† Crystallographic data of $\mathbf{H_2L}$ can also be obtained from the CCDC using the 2402446.

Authors contributions

"Tesfa Oluma Fufa" was the primary author responsible for the experimental work, manuscript drafting, data analysis and interpretation. "Hui Li" was a corresponding author who provided continuous supervision and aided successful completion of the research. "Hongwei Ma" was the 2nd author and made significant contributions to the crystallographic work and manuscript revisions. Also, the 3rd, 4th & 5th authors actively participated in the data collection and manuscript revisions.

Conflicts of interest

There are no conflicts to declare.

Acknowledgements

This work was supported by the National Natural Science Foundation of China (No. 21071018, 21271026, 21471017). Therefore, for this work, our heart gratitude is to the Chinese Scholarship Council and to the Analysis and Testing Centre of the Beijing Institute of Technology.

References

1 M. Zhao, B. Li, H. Zhang and F. Zhang, Activatable fluorescence sensors for *in vivo* bio-detection in the second near-infrared window, *Chem. Sci.*, 2021, **12**, 3448–3459.
2 K. Rurack, Flipping the light switch 'ON'–the design of sensor molecules that show cation-induced fluorescence enhancement with heavy and transition metal ions, *Spectrochim. Acta, Part A*, 2001, **57**, 2161–2195.
3 A. P. De Silva, H. N. Gunaratne, T. Gunnlaugsson, A. J. Huxley, C. P. McCoy, J. T. Rademacher and T. E. Rice, Signaling recognition events with fluorescent sensors and switches, *Chem. Rev.*, 1997, **97**, 1515–1566.
4 L. Chen, C. Yan, M. Pan, H.-P. Wang, Y.-N. Fan and C.-Y. Su, Multi-Mode White Light Emission in a ZnII Coordination Polymer from Excited-State Intramolecular Proton Transfer (ESIPT) Ligands, *Eur. J. Inorg. Chem.*, 2016, **2016**, 2676–2680.
5 J. Seo, S. Kim and S. Y. Park, Strong solvatochromic fluorescence from the intramolecular charge-transfer state

created by excited-state intramolecular proton transfer, *J. Am. Chem. Soc.*, 2004, **126**, 11154–11155.

6 S. Paul and P. Barman, Exploring diaminomaleonitrile-derived Schiff base ligand and its complexes: Synthesis, characterization, computational insights, biological assessment, and molecular docking, *J. Mol. Struct.*, 2024, **1296**, 136941.

7 Q. Meng, P. Zhou, F. Song, Y. Wang, G. Liu and H. Li, Controlled fluorescent properties of Zn (II) salen-type complex based on ligand design, *CrystEngComm*, 2013, **15**, 2786–2790.

8 C. Justin Dhanaraj and M. Sivasankaran Nair, Synthesis, characterization, and antimicrobial studies of some Schiff-base metal (II) complexes, *J. Coord. Chem.*, 2009, **62**, 4018–4028.

9 M. J. MacLachlan, M. K. Park and L. K. Thompson, Coordination compounds of Schiff-base ligands derived from diaminomaleonitrile (DMN): mononuclear, dinuclear, and macrocyclic derivatives, *Inorg. Chem.*, 1996, **35**, 5492–5499.

10 D. Wöhrle, H. Bohlen and H.-W. Rothkopf, Polymeric schiff's base chelates and their precursors, 4. Syntheses of schiff's base chelates from diaminomaleonitrile and investigation of their activity for the valence isomerisation of quadricyclane to norbornadien, *Macromol. Chem. Phys.*, 1983, **184**, 763–778.

11 R. K. Sharma and M. Agrawal, Biological effects of heavy metals: an overview, *J. Environ. Biol.*, 2005, **26**, 301–313.

12 H. Liu, S. Ding, Q. Lu, Y. Jian, G. Wei and Z. Yuan, A versatile Schiff Base Chemosensor for the determination of trace Co2+, Ni2+, Cu2+, and Zn2+ in the water and its bioimaging applications, *ACS Omega*, 2022, **7**, 7585–7594.

13 F. Edition, *Guidelines for Drinking-Water Quality*, WHO chronicle, 2011, vol. 38, pp. 104–108.

14 A. Gonzales, M. Firmino, C. S. Nomura, F. R. P. Rocha, P. de Oliveira and I. Gaubeur, Peat as a natural solid-phase for copper preconcentration and determination in a multicommuted flow system coupled to flame atomic absorption spectrometry, *Anal. Chim. Acta*, 2009, **636**, 198–204.

15 S. Bhunia, S. Halder, K. Naskar, B. Dutta, D. Sahoo, K. Jana and C. Sinha, Spectrophotometric determination of trace amount of total FeII/FeIII and live cell imaging of a carboxylato Zn (II) coordination polymer, *Inorg. Chem.*, 2022, **61**, 19790–19799.

16 S. Mukherjee, A. Ghati and G. Paul, An ultraviolet–visible spectrophotometric approach to establish a method for determining the presence of rhodamine B in food articles, *ACS Food Sci. Technol.*, 2021, **1**, 1615–1622.

17 M. Soylak, Y. E. Unsal, E. Yilmaz and M. Tuzen, Determination of rhodamine B in soft drink, waste water and lipstick samples after solid phase extraction, *Food Chem. Toxicol.*, 2011, **49**, 1796–1799.

18 Y. E. Unsal, M. Soylak and M. Tuzen, Dispersive liquid–liquid microextraction–spectrophotometry combination for determination of rhodamine B in food, water, and environmental samples, *Desalin. Water Treat.*, 2015, **55**, 2103–2108.

19 P. Pallavi, V. Kumar, M. W. Hussain and A. Patra, Excited-state intramolecular proton transfer-based multifunctional solid-state emitter: a fluorescent platform with "write-erase-write" function, *ACS Appl. Mater. Interfaces*, 2018, **10**, 44696–44705.

20 T.-B. Ren, W. Xu, W. Zhang, X.-X. Zhang, Z.-Y. Wang, Z. Xiang, L. Yuan and X.-B. Zhang, A general method to increase stokes shift by introducing alternating vibronic structures, *J. Am. Chem. Soc.*, 2018, **140**, 7716–7722.

21 S. Park, O.-H. Kwon, S. Kim, S. Park, M.-G. Choi, M. Cha, S. Y. Park and D.-J. Jang, Imidazole-based excited-state intramolecular proton-transfer materials: synthesis and amplified spontaneous emission from a large single crystal, *J. Am. Chem. Soc.*, 2005, **127**, 10070–10074.

22 O. McCubbin Stepanic, J. Ward, J. E. Penner-Hahn, A. Deb, U. Bergmann and S. DeBeer, Probing a silent metal: a combined X-ray absorption and emission spectroscopic study of biologically relevant zinc complexes, *Inorg. Chem.*, 2020, **59**, 13551–13560.

23 J. E. Penner-Hahn, Characterization of "spectroscopically quiet" metals in biology, *Coord. Chem. Rev.*, 2005, **249**, 161–177.

24 K. Sarkar, K. Dhara, M. Nandi, P. Roy, A. Bhaumik and P. Banerjee, Selective zinc (II)-ion fluorescence sensing by a functionalized mesoporous material covalently grafted with a fluorescent chromophore and consequent biological applications, *Adv. Funct. Mater.*, 2009, **19**, 223–234.

25 S. P. Anthony, Organic solid-state fluorescence: strategies for generating switchable and tunable fluorescent materials, *ChemPlusChem*, 2012, **77**, 518–531.

26 J. P. Costes, J. F. Lamere, C. Lepetit, P. G. Lacroix, F. Dahan and K. Nakatani, Synthesis, crystal structures, and nonlinear optical (NLO) properties of new Schiff-base nickel (II) complexes. Toward a new type of molecular switch?, *Inorg. Chem.*, 2005, **44**, 1973–1982.

27 K. Aich, S. Goswami, S. Das, C. D. Mukhopadhyay, C. K. Quah and H.-K. Fun, Cd2+ triggered the FRET "ON": a new molecular switch for the ratiometric detection of Cd2+ with live-cell imaging and bound X-ray structure, *Inorg. Chem.*, 2015, **54**, 7309–7315.

28 O. V. Dolomanov, L. J. Bourhis, R. J. Gildea, J. A. K. Howard and H. Puschmann, OLEX2: a complete structure solution, refinement and analysis program, *J. Appl. Crystallogr.*, 2009, **42**, 339–341.

29 G. M. Sheldrick, SHELXT–Integrated space-group and crystal-structure determination, *Acta Crystallogr., Sect. A:Found. Adv.*, 2015, **71**, 3–8.

30 G. M. Sheldrick, Crystal structure refinement with SHELXL, *Acta Crystallogr., Sect. C:Struct. Chem.*, 2015, **71**, 3–8.

31 P. G. Lacroix, S. Di Bella and I. Ledoux, Synthesis and second-order nonlinear optical properties of new copper (II), nickel (II), and zinc (II) Schiff-base complexes. Toward a role of inorganic chromophores for second harmonic generation, *Chem. Mater.*, 1996, **8**, 541–545.

32 X. Chen, J. Zhang, H. Zhang, Z. Jiang, G. Shi, Y. Li and Y. Song, Preparation and nonlinear optical studies of a novel thermal stable polymer containing azo chromophores in the side chain, *Dyes Pigm.*, 2008, **77**, 223–228.

33 C. Anitha, C. Sheela, P. Tharmaraj and R. Shanmugakala, Studies on Synthesis and Spectral Characterization of Some Transition Metal Complexes of Azo-Azomethine Derivative of Diaminomaleonitrile, *Int. J. Inorg. Chem.*, 2013, **2013**, 436275.

34 A. R. Katritzky, D. C. Fara, H. Yang, K. Tämm, T. Tamm and M. Karelson, Quantitative measures of solvent polarity, *Chem. Rev.*, 2004, **104**, 175–198.

35 P. Muthukumar, M. Surya, M. Pannipara, A. G. Al-Sehemi, D. Moon and S. Philip Anthony, Easily Accessible Schiff Base ESIPT Molecules with Tunable Solid State Fluorescence: Mechanofluorochromism and Highly Selective Co2+ Fluorescence Sensing, *ChemistrySelect*, 2020, **5**, 3295–3302.

36 A. Bhattacharyya, S. K. Mandal and N. Guchhait, Imine–amine tautomerism *vs.* keto–enol tautomerism: Acceptor basicity dominates over acceptor electronegativity in the ESIPT process through a six-membered intramolecular H-bonded network, *J. Phys. Chem. A*, 2019, **123**, 10246–10253.

37 S. Sinha, B. Chowdhury and P. Ghosh, A highly sensitive ESIPT-based ratiometric fluorescence sensor for selective detection of Al3+, *Inorg. Chem.*, 2016, **55**, 9212–9220.

38 J. Junyong, L. H. Yong, L. Wenjun, O. András, C. Chun-Hsing and L. Dongwhan, Reactivity-Based Detection of Copper (II) Ion in Water: Oxidative Cyclization of Azoaromatics as Fluorescence Turn-On Signaling Mechanism.

39 J. Lakowicz, *Principles of fluorescence spectroscopy*, Springer, NY, 3rd edn, 2006, pp. 205–235.

40 F. A. Chipem and G. Krishnamoorthy, Temperature effect on dual fluorescence of 2-(2′-Hydroxyphenyl) benzimidazole and its nitrogen substituted analogues, *J. Phys. Chem. B*, 2013, **117**, 14079–14088.

41 A. Heller and D. L. Williams, Intramolecular proton transfer reactions in excited fluorescent compounds, *J. Phys. Chem.*, 1970, **74**, 4473–4480.

42 R. F. Kubin and A. N. Fletcher, Fluorescence quantum yields of some rhodamine dyes, *J. Lumin.*, 1982, **27**, 455–462.

43 G. A. Crosby and J. N. Demas, Measurement of photoluminescence quantum yields. Review, *J. Phys. Chem.*, 1971, **75**, 991–1024.

44 H.-T. Feng, J. Zeng, P.-A. Yin, X.-D. Wang, Q. Peng, Z. Zhao, J. W. Lam and B. Z. Tang, Tuning molecular emission of organic emitters from fluorescence to phosphorescence through push-pull electronic effects, *Nat. Commun.*, 2020, **11**, 2617.

45 J.-B. Li, H.-W. Zheng, M. Wu, Q.-F. Liang, D.-D. Yang, X.-J. Zheng and H.-W. Tan, Multistimulus Response of Two Tautomeric Zn (II) Complexes and Their White-Light Emission Based on Different Mechanisms, *Inorg. Chem.*, 2021, **60**, 17677–17686.

46 W. Kemp, *Organic Spectroscopy*, Bloomsbury Publishing, 2017.

47 S. Luangphai, J. Fongsiang, P. Thuptimdang, S. Buddhiranon and K. Chanawanno, Colorimetric Cu2+ Detection of (1 E, 2 E)-1, 2-Bis ((1 H-pyrrol-2-yl) methylene) hydrazine Using a Custom-Built Colorimeter, *ACS Omega*, 2022, **7**, 44448–44457.

48 L. Zou, B. Yan, D. Pan, Z. Tan and X. Bao, A colorimetric and absorption ratiometric anion sensor based on indole & hydrazide binding units, *Spectrochim. Acta, Part A*, 2015, **148**, 78–84.

49 V. P. Gupta and T. Poonam, Conformational and vibrational studies of isomeric hydrogen cyanide tetramers by quantum chemical methods, *Spectrochim. Acta, Part A*, 2012, **89**, 55–66.

50 A. El Majzoub, C. Cadiou, I. Déchamps-Olivier, B. Tinant and F. Chuburu, Cyclam-methylbenzimidazole: a selective OFF-ON fluorescent sensor for Zinc, *Inorg. Chem.*, 2011, **50**(9), 4029–4038.

51 R. Bawa, S. Negi, B. Singh, B. Pani and R. Kumar, A pyridine dicarboxylate based hydrazone Schiff base for reversible colorimetric recognition of Ni 2+ and PPi, *RSC Adv.*, 2023, **13**(23), 15391–15400.